

Hydrogenation of CO₂ to higher alcohols on an efficient Cr-modified CuFe catalyst

Qian Zhang ^{a,b}, Sen Wang ^{a,*}, Rui Geng ^{a,b}, Pengfei Wang ^a, Mei Dong ^a, Jianguo Wang ^{a,b}, Weibin Fan ^{a,*}

^a State Key Laboratory of Coal Conversion, Institute of Coal Chemistry, Chinese Academy of Sciences, Taiyuan, Shanxi 030001, PR China

^b University of the Chinese Academy of Sciences, Beijing 100049, PR China



ARTICLE INFO

Keywords:
CO₂ hydrogenation
Higher alcohol
CuFe catalyst
Cr modification
Reaction mechanism

ABSTRACT

CO₂ hydrogenation to higher alcohols (C₂₊OH) is a promising approach to achieve carbon recycling, but it is a challenge due to complex reaction network. Herein, various Cr-modified CuFe (Cr(x)-CuFe) catalysts were prepared, and their catalytic performance and reaction mechanism in CO₂ hydrogenation to C₂₊OH were investigated. Introduction of small amounts of Cr enhances the interaction between Cu and Fe species, which alleviates CO over-dissociation and inhibits generation of iron carbides. In contrast, more acetate and acetaldehyde intermediates are produced via promoting the reaction of CH_x with non-dissociated CO. Cr(1%)-CuFe showed CO₂ conversion, C₂₊OH selectivity and space-time yield (STY) as high as 38.4%, and 29.2% and 104.1 mg g_{cat}⁻¹ h⁻¹, at 320 °C, 4.0 MPa and GHSV of 6000 mL g_{cat}⁻¹ h⁻¹. Interestingly, C₂₊OH STY was further elevated to 268.5 mg g_{cat}⁻¹ h⁻¹, with a catalytic lifetime of at least 120 h, when GHSV was increased to 48000 mL g_{cat}⁻¹ h⁻¹.

1. Introduction

The combustion of large amounts of fossil fuels, e.g. coal and petroleum, causes excessive CO₂ emission into the atmosphere. In February 2023, the global CO₂ level in the atmosphere has reached 418.3 ppm [1,2], which leads to serious greenhouse effect, ocean acidification and other environmental problems [3,4]. Efficient conversion of CO₂ into high-value methane, gasoline, olefins, aromatics and oxygenates, etc. can not only reduce CO₂ emission and promote carbon neutrality, but also provide a new approach to produce fuels and commodity chemicals [5–10]. Higher alcohols (C₂₊OH) are important building blockings, and have been widely used as eco-friendly additives, solvents and surfactants in modern chemical industry [11–13].

However, selective hydrogenation of CO₂ to higher alcohols (C₂₊OH) is a challenge due to the high stability of CO₂ molecule and the complexity of C-C coupling reactions [14–18]. Llorca and co-workers anchored single Pd atoms onto Fe₂O₃ support, which showed an ethanol selectivity of 97.5%, along with the ethanol space time yield (STY) of 413 mmol_{ethanol} g_{Pd}⁻¹ h⁻¹, at 300 °C and 0.1 MPa [19], although the CO₂ conversion is only 0.3%. They assumed that the interaction between Pd single atom and Fe₃O₄ support play a vital role in C-C coupling. A more active catalyst is metallic Pt nanoparticles (NPs)

supported on Co₃O₄ nanoplates (Pt/Co₃O₄-p) that gave a higher alcohols STY of 0.56 mmol g_{cat}⁻¹ h⁻¹ at 200 °C and 2.0 MPa. The synergic effect of Pt-Co nanoparticles and the surface oxygen vacancies of Co₃O_{4-x} promoted the activations of H₂ and CO₂, and thus, enhancing the formation of C₂₊OH [20]. Recently, CeO₂-supported Pd dimer was found to exhibit an ethanol selectivity as high as 99.2% and a STY of 45.6 g_{ethanol} g_{Pd}⁻¹ h⁻¹ at 240 °C, 3.0 MPa and 3000 mL g_{cat}⁻¹ h⁻¹ [21]. This is due to the unique Pd₂O₄ configuration that can directly dissociate CO₂ into CO and significantly promote the reaction of CH_x and CO. Nevertheless, these noble metal-based catalysts are very expensive, limiting the large-scale applications.

In contrast, cheap and abundant CuFe-based catalysts receive a lot of attention in CO₂ hydrogenation to higher alcohols [22–29]. Sun and co-workers found that Na-modified CuFe catalyst prepared by the physical sputtering method showed high activity in CO₂ hydrogenation due to enhancement of CO₂ adsorption and Fe reduction and carbonization. The CO₂ conversion, ethanol selectivity and STY reached 32.3%, ~17% and 153 mg g⁻¹ h⁻¹ at 310 °C, 3.0 MPa and 28,800 mL g⁻¹ h⁻¹ [22]. At optimum condition, CuZnAl/K-CuMgZnFe bifunctional catalyst gave the C₂₊OH selectivity and STY of 17.4% and 106.5 mg g_{cat}⁻¹ h⁻¹ [25]. Generally, higher alcohols are formed via the CO-intermediate route over CuFe-based catalysts. First, CO is generated through reverse

* Corresponding authors.

E-mail addresses: wangsen@sxicc.ac.cn (S. Wang), fanwb@sxicc.ac.cn (W. Fan).

water-gas shift (RWGS) reaction on Cu sites. Then, a part of them is dissociated and hydrogenated to CH_x intermediates over iron carbide (FeC_x). The CH_x species are subsequently coupled into hydrocarbons or interacted with non-dissociated CO to form higher alcohols on $\text{Cu}-\text{FeC}_x$ interface [14,22]. This suggests that the CH_x-CH_x coupling reaction should be inhibited by enhancing the $\text{Cu}-\text{FeC}_x$ interaction, which promotes formation of more $\text{Cu}-\text{FeC}_x$ interfaces.

Here, the CuFe oxides was modified with Cr by the sol-gel method. It shows CO_2 conversion of 38.4% and C_{2+}OH selectivity and STY of 29.2% and 104.1 mg $\text{g}_{\text{cat}}^{-1} \text{h}^{-1}$ at 320 °C, 4.0 MPa and GHSV of 6000 mL $\text{g}_{\text{cat}}^{-1} \text{h}^{-1}$. The C_{2+}OH STY can be further increased to 268.5 mg $\text{g}_{\text{cat}}^{-1} \text{h}^{-1}$ by increasing GHSV to 48000 mL $\text{g}_{\text{cat}}^{-1} \text{h}^{-1}$. In situ spectroscopy and theoretical calculation results reveal that doping proper amounts of Cr in CuFe catalyst enhances the interaction of Cu and Fe species, which promotes formation of more acetate and acetaldehyde intermediates, and hence, of more C_{2+}OH .

2. Experimental section

2.1. Catalyst preparation

Various Cr-modified CuFe catalysts with different Cr content ($\text{Cr}(x)$ -CuFe, x represents the Cr loading, $x = 0, 0.5, 0.75, 1, 1.25, 2$ or 3%) were synthesized using sol-gel method. Typically, designed amounts of copper nitrate ($\text{Cu}(\text{NO}_3)_2 \bullet 3 \text{H}_2\text{O}$), iron nitrate ($\text{Fe}(\text{NO}_3)_3 \bullet 9 \text{H}_2\text{O}$), chromium nitrate ($\text{Cr}(\text{NO}_3)_3 \bullet 9 \text{H}_2\text{O}$) and potassium nitrate (KNO_3) were first dissolved in water and stirred at 25 °C for 3 h. After that, certain amount of glucose was added and the solution was further stirred at 80 °C for another 6 h until the water completely evaporated. Finally, the colloid solids were dried in the oven at 120 °C for 12 h, and then calcinated at 500 °C for 6 h in air. The atomic ratio of Cu/Fe is 1/1, with the K loading of 2 wt% in all of the Cr(x)-CuFe catalysts.

2.2. Catalyst characterization

X-ray diffraction (XRD) patterns of various Cr(x)-CuFe catalysts were obtained on Bruker D8 Advance X-ray powder instrument at the Cu K α radiation (40 kV and 40 mA). XRD patterns were scanned ranging from 5 to 80° (4° min^{-1}).

N_2 adsorption isotherms of various samples were operated on Micromeritics TriStar II 3020 equipment. Before testing at -196 °C, 100 mg catalysts were first pre-treated at 300 °C for 5 h. BET, t-plot and BJH methods were adopted to evaluate the surface area, pore volume and the pore size distribution of catalysts.

JEM-2100 F (JEOL) field emission-transmission electron microscope was used to obtain the high-resolution transmission electron microscopy images (HRTEM) and the energy-dispersive X-ray (EDX) elemental mapping results.

Fe 2p, Cu 2p and Cr 2p X-ray photoelectron spectroscopy (XPS) were conducted on AXIS ULTRA DLD under vacuum using the monochromatic Al K α X-ray source ($\hbar\nu = 1486.6 \text{ eV}$). The results were corrected by C 1 s at 284.6 eV. ^{57}Fe Mössbauer spectra of samples were recorded on an SEE Co W304 Mössbauer spectrometer at room temperature, using a $^{57}\text{Co}/\text{Rh}$ source in transmission geometry. Low-energy ion scattering (LEIS) spectra of various catalysts were obtained on QTAC100 instrument with Ne as the excitation source.

Fe K-edge XAFS measurement in transmission mode was conducted at the BL11B beamlines at the Shanghai Synchrotron Radiation Facility (SSRF). Fe foil, FeO , Fe_2O_3 and Fe_3O_4 were used as the referenced samples. The XAFS data was treated with the aid of IFEFFIT software for calibrating the background, pre-edge and post-edge lines.

Temperature-programmed reduction of H_2 (H_2 -TPR) was carried out on Micromeritics Autochem 2920 equipment. 50 mg catalysts were placed in the U-type quartz tube and treated under He flow at 300 °C for 60 min. After cooling to 50 °C, 5% H_2/Ar flow was introduced with elevation of temperature from 50 °C to 800 °C ($10^\circ \text{C min}^{-1}$). The signals

were then detected by TCD.

Temperature-programmed desorption of CO (CO-TPD) was also conducted on the same Micromeritics Autochem 2920. 50 mg catalysts were first pre-treated as that of H_2 -TPR. The temperature was subsequently cooled to 50 °C for CO saturation adsorption for 30 min, and then, the gas was converted into He to purge the residual CO. After that, the sample was heated from 50 °C to 800 °C ($10^\circ \text{C min}^{-1}$). The signal was detected by TCD. The H_2 -TPD and CO_2 -TPD were also measured using the same Micromeritics Autochem 2920. The procedures are similar to those employed for CO-TPD except that CO was replaced with H_2 or CO_2 .

Temperature programmed surface reaction (TPSR) of CO hydrogenation was performed on a microreactor. 100 mg samples were loaded in U-type tube and treated at 400 °C for 2 h in H_2 (30 mL min^{-1}). The temperature was then decreased to 30 °C and the CO and H_2 mixture (H_2/CO of 2:1) was introduced, along with elevation of temperature from 30 °C to 350 °C at 4° min^{-1} . The effluents were detected by on-line MS (Hiden Analytical HPR-20 R&D).

In situ DRIFTS measurements were conducted on a Bruker VERTEX 80 infrared spectrometer. First, 50 mg catalysts were treated in H_2 (30 mL min^{-1}) at 400 °C for 120 min, and subsequently cooled to 300 °C to obtain the background spectrum. Then, CO_2 and H_2 gases (H_2/CO_2 of 3:1, 40 mL min^{-1}) were continuously introduced into the reaction cell and the spectra were collected in the range of 4000–1000 cm^{-1} by accumulating 64 scans.

CO-DRIFTS were conducted on a Bruker VERTEX 80 infrared spectrometer. 50 mg catalyst were first reduced at 400 °C for 120 min in a H_2 flow (30 mL min^{-1}). Then, it was cooled to 30 °C in an Ar flow (50 mL min^{-1}) to collect the background spectra. After that, CO was introduced at 30 °C for adsorption of 30 min. Finally, the gas was switched to Ar (10 mL min^{-1}) and the spectra were collected at different times.

2.3. Catalytic evaluation

The catalytic reactions were conducted in a high-pressure fixed-bed reactor (10 mm inner diameter of the reaction tube). Typically, 0.4 g samples (20–40 mesh) were placed in the middle of reaction tube and other parts were filled with quartzite. Before measurement, the samples were pre-treated at 400 °C and 1 atm for 120 min in H_2 (30 mL min^{-1}). After cooling to reaction temperature, the feeding gas (H_2 to CO_2 ratio of 3:1) was introduced and the reaction was performed at 4.0 MPa, GHSV of 6000 mL $\text{g}^{-1} \text{h}^{-1}$ and 300 °C, unless otherwise stated.

The effluent products were on-line detected using Agilent 7890 A gas chromatograph (GC) having two FIDs and one TCD directors. The condensed liquid phase was analyzed using another Agilent 7890 A GC with one TCD and one FID.

The following equations were used to calculate the CO_2 conversion ($x(\text{CO}_2)$) and CO selectivity ($s(\text{CO})$):

$$x(\text{CO}_2) = \frac{N(\text{CO}_2, \text{in}) - N(\text{CO}_2, \text{out})}{N(\text{CO}_2, \text{in})} \times 100\%$$

$$s(\text{CO}) = \frac{N(\text{CO}, \text{out})}{N(\text{CO}_2, \text{in}) - N(\text{CO}_2, \text{out})} \times 100\%$$

where $N(\text{CO}_2, \text{in})$ represents the molar content of CO_2 feed, while that of $N(\text{CO}_2, \text{out})$ and $N(\text{CO}, \text{out})$ are short for molar contents of CO_2 and CO in products, respectively. The selectivities of alcohols (COH) and hydrocarbons ($\text{C}_i\text{H}_{j,i}$) in effluents were evaluated as [23,24].

$$s(\text{COH}) = \frac{n(\text{COH})}{\sum i \bullet n(\text{C}_i\text{H}_{j,i}) + n(\text{COH})} \times 100\%$$

$$s(\text{C}_i\text{H}_{j,i}) = \frac{i \bullet n(\text{C}_i\text{H}_{j,i})}{\sum i \bullet n(\text{C}_i\text{H}_{j,i}) + n(\text{COH})} \times 100\%$$

where $n(\text{C}_i\text{H}_{j,i})$ and $n(\text{COH})$ represent the molar contents of hydrocarbon

products (C_iH_{jx}) and alcohols, respectively. The catalytic results after reaction of ~ 24 h were generally used for comparison with carbon molar balance around 95%–100%.

2.4. DFT calculation

DFT calculations were conducted on Vienna Ab Initio Simulation Package (VASP) [30]. The electron-ion interaction was described using projector augmented wave (PAW) method; the electron exchange and correlation energies were calculated with the generalized gradient approximation in the Perdew-Burke-Ernzerhof functional (GGA-PBE) [31]. The plane wave cutoff energy was 400 eV, with the total electronic energy convergence of 1×10^{-5} eV and the remaining total force below 0.05 eV/Å. The Monkhorst Pack mesh k-point of $(2 \times 2 \times 1)$ was used in DFT calculations.

A $p(3 \times 3)$ supercell with three layers of metallic Cu was built to simulate Cu(111) face with Fe_5C_2 and CrO_x placed on the surface (Fig. S1) according to the method reported by Mori and co-workers [32]. During geometry optimization, reactant molecules and Fe_5C_2 and CrO_x clusters were fully relaxed, while the metallic Cu species was fixed at their bulk positions. The spin polarization calculation was conducted with ISPIN setting of 2. The explicit valence electrons for different atoms were assumed to be $Cu-3d^{10}4s^1$, $Fe-3d^64s^2$, $C-2s^22p^2$, $O-2s^22p^4$, $Cr-3d^54s^1$ and $H-1s^1$. Transition-state structures were obtained using climbing image nudged elastic-band (CI-NEB) method [33]. The energy barrier and reaction energy are the energy difference between transition state and initial state, and between final state and initial state, respectively.

3. Results and discussion

3.1. Catalytic performance of $Cr(x)$ -CuFe catalysts

The catalytic evaluation of $Cr(x)$ -CuFe samples for CO_2 hydrogenation to higher alcohols ($C_{2+}OH$) was first performed at 300 °C and 4.0 MPa. Fig. 1 shows that the CuFe catalyst gives CO_2 conversion, $C_{2+}OH$ selectivity and $C_{2+}OH$ STY of 25.5%, 18.9% and $39.2 \text{ mg g}_{\text{cat}}^{-1} \text{ h}^{-1}$. Introduction of 1 wt% Cr in the CuFe catalyst significantly promotes the formation of higher alcohols. The CO_2 conversion, $C_{2+}OH$ selectivity and $C_{2+}OH$ STY are increased to 33.5%, 24.9% and $76.3 \text{ mg g}_{\text{cat}}^{-1} \text{ h}^{-1}$ at the same conditions. In addition, the CO selectivity is decreased from 23.6% to 16.0%. Nevertheless, a further elevation of the Cr content not only lowers both the $C_{2+}OH$ selectivity and its STY, but also raises CO selectivity. The variation of CO selectivity with the $C_{2+}OH$ content indicates that CO is an important intermediate for synthesis of higher alcohols [24,28]. Table S1 shows that addition of excessive amounts of Cr species leads to a serious deposition of Cr species on the

CuFe catalyst surface, and as a result, hindering the interaction of CH_x with non-dissociated CO over Cu-FeC_x interface.

Since these catalysts were prepared by the sol-gel method with glucose serving as the complexing agent, the possible influence of residual carbon species was further considered. Table S2 shows that the residual carbon species in all the samples have similar content, being in the range of 0.16–0.27 wt%, as a result of the same preparation conditions. Such a low content of residual carbon species suggests that they should not be the primary reason for their considerably different catalytic performance. To confirm this deduction, the calcination temperature of dried Cr(1%)-CuFe sample was decreased from 500 °C to 400 °C, along with the increase of the residual carbon species content from 0.21 wt% to 0.27 wt%. Clearly, no significant effect was observed on the catalytic performance in CO_2 hydrogenation (Fig. S2).

In addition, all the catalysts contained the same loading of K, as alkali metals are generally necessary promoters for CuFe-based catalysts in CO_2 hydrogenation to higher alcohols. This is because alkali metals can suppress over-hydrogenation, thus, inhibiting the formation of methane and C_{2+} alkanes. Furthermore, they can enhance catalyst alkalinity, promoting CO_2 adsorption and activation [24]. These functions are confirmed by the catalytic result obtained over the Cr (1%)-CuFe without K additive; the selectivity to C_2^{\pm} - C_4^{\pm} olefins and that to higher alcohols are largely decreased, along with generation of much more methane and C_2 - C_4 alkanes over Cr(1%)-CuFe without K additive (Fig. S3).

The catalytic performance of Cr(1%)-CuFe in CO_2 hydrogenation to higher alcohols is related to the reaction temperature. With the elevation of temperature from 280 °C to 320 °C, the selectivity and the STY of $C_{2+}OH$ are gradually increased from 18.3% and $26.4 \text{ mg g}_{\text{cat}}^{-1} \text{ h}^{-1}$ to 29.2% and $104.1 \text{ mg g}_{\text{cat}}^{-1} \text{ h}^{-1}$, respectively, while the CO selectivity is decreased from 29.4% to 14.8% (Fig. 2(a) and (b)). However, further increase of the reaction temperature to 340 °C leads to the decrease of both $C_{2+}OH$ selectivity and STY to 23.6% and $89.2 \text{ mg g}_{\text{cat}}^{-1} \text{ h}^{-1}$, respectively, along with generation of more methane, light alkanes (C_2^0 - C_4^0) and light alkenes (C_2^{\pm} - C_4^{\pm}), despite that the CO_2 conversion is elevated to 41.4%. This is because too-high temperature induces the rapid dissociation of CO intermediate to produces more CH_x species, which are further hydrogenated or coupled to methane or C_{2+} hydrocarbons [15].

Increasing the reaction pressure can rise the CO_2 conversion, and the selectivity and STY of $C_{2+}OH$, but decrease the CO selectivity, as CO_2 hydrogenation to higher alcohols is volume-reduced reaction and higher pressure is thermodynamically favorable for the formation of higher alcohols [25]. At 320 °C, 4.0 MPa and $6000 \text{ mL g}^{-1} \text{ h}^{-1}$, the CO_2 conversion reaches 38.4%, with the selectivity and the STY of $C_{2+}OH$ of 29.2% and $104.1 \text{ mg g}_{\text{cat}}^{-1} \text{ h}^{-1}$, respectively (Figs. 2(c) and 2(d)). The CO_2 conversion is gradually decreased with the increase of space velocity,

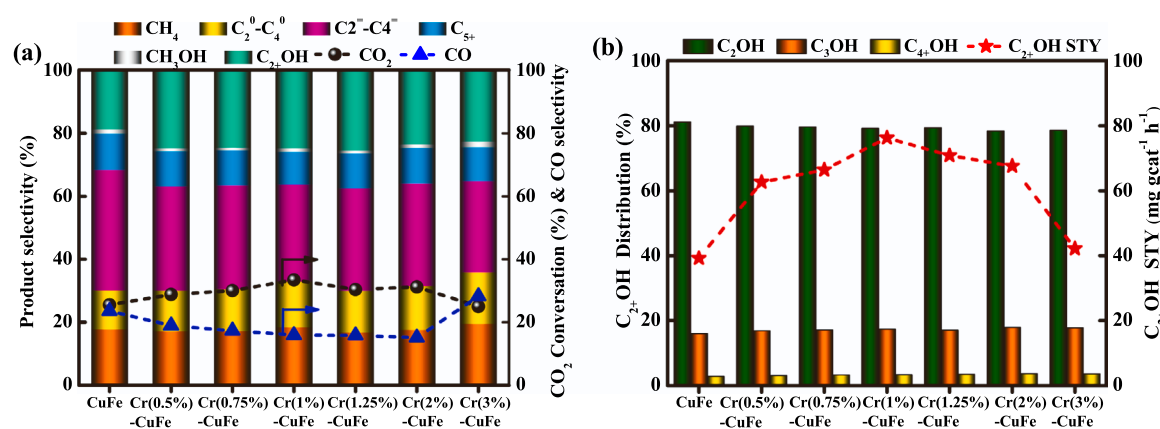


Fig. 1. Catalytic performance of $Cr(x)$ -CuFe catalysts in hydrogenation of CO_2 to higher alcohols. Reaction conditions: 300 °C, 4.0 MPa, GHSV of $6000 \text{ mL g}_{\text{cat}}^{-1} \text{ h}^{-1}$ and $H_2/CO_2 = 3/1$.

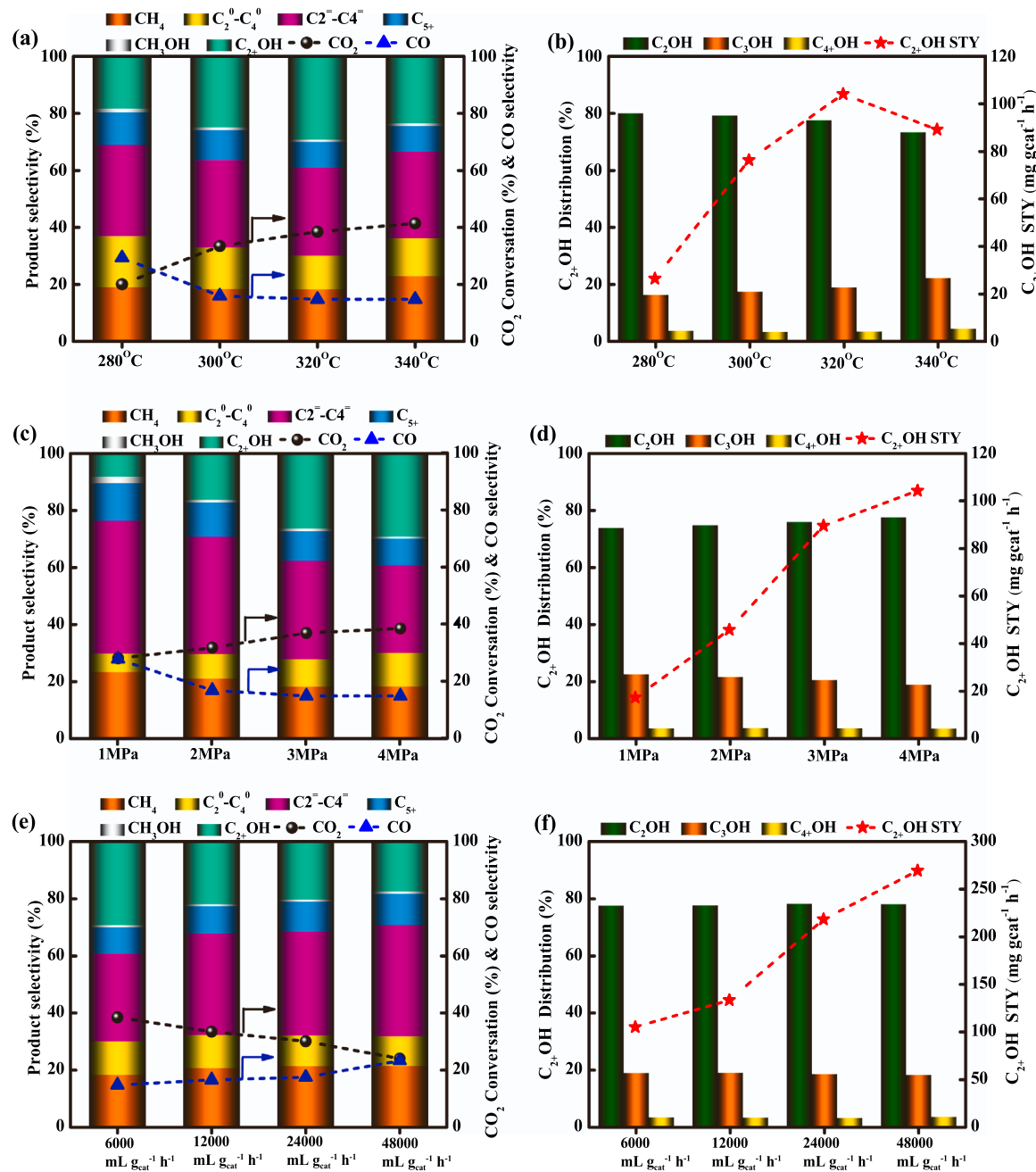


Fig. 2. Influence of reaction temperature ((a) and (b)), pressure ((c) and (d)), and space velocity ((e) and (f)) on the catalytic performance of Cr(1%)-CuFe catalyst in CO_2 hydrogenation to higher alcohols.

due to the shortening of contact time. Nevertheless, the C_{2+}OH STY reaches as high as $268.5 \text{ mg g}^{-1} \text{ h}^{-1}$ at 320°C , 4.0 MPa and $48000 \text{ mL g}^{-1} \text{ h}^{-1}$ (Fig. 2(e) and (f)), indicating the high intrinsic activity of Cr(1%)-CuFe for the formation of higher alcohols. To the best of our knowledge, such high C_{2+}OH STY makes Cr(1%)-CuFe surpass most of other reported CuFe-based catalysts in CO_2 hydrogenation to C_{2+}OH (Fig. 3 and Table S3).

The Cr(1%)-CuFe catalyst also presents high catalytic stability in CO_2 hydrogenation to higher alcohols. After reaction of 120 h , the CO_2 conversion, and the selectivity and STY of C_{2+}OH are well maintained at around 35.8% , 23.3% and $82.5 \text{ mg g}^{-1} \text{ h}^{-1}$, respectively at 320°C , 4.0 MPa and $6000 \text{ mL g}^{-1} \text{ h}^{-1}$ (Fig. S4). Even at higher space velocity of 24000 and $48000 \text{ mL g}^{-1} \text{ h}^{-1}$, the C_{2+}OH STY on Cr(1%)-CuFe keeps nearly unchanged within 120 h (Figs. 4 and S5). All of these results suggest the potential of Cr(1%)-CuFe catalyst for practical application.

3.2. Catalytic characterization of Cr(x)-CuFe catalysts

The crystal structures of various Cr(x)-CuFe catalysts were analyzed by XRD patterns. As depicted in Fig. 5(a), the diffraction peaks at 20 of 35.7° , 39.0° and 49.0° , corresponding to the $(1\ 1\ -1)$, $(1\ 1\ 1)$ and $(2\ 0\ -2)$ crystal facets of CuO , are detected, while that of Fe-related species is invisible, indicating the amorphous phase of FeO_x species, being in line with previous observations on CuFe catalysts [24,25]. It can be verified by the HR-TEM images that only the lattice fringe of CuO (0.259 nm) is clearly identified, whereas the crystal phase of FeO_x is absent over Cr(x)-CuFe samples (Figs. 5(d) and S6). Introduction of small amount of Cr has smaller effect on the crystalline structure of CuFe catalysts (Fig. 5(a)), although the average nanoparticle (NP) size of samples is increased from 5.8 nm to 13.5 nm with increasing Cr content from 0 (CuFe sample) to 3% (Cr(3%)-CuFe) (Figs. 5(c) and S7). The

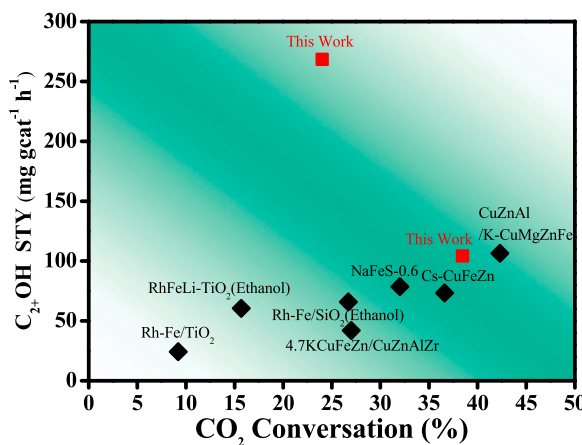


Fig. 3. Comparison of the space-time yield (STY) of $\text{C}_2\text{+OH}$ obtained in this work with the results in references.

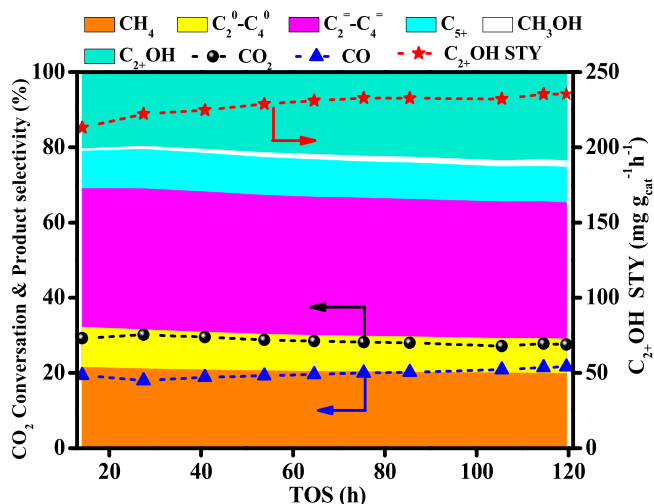


Fig. 4. Catalytic stability test of Cr(1%)-CuFe catalyst in CO_2 hydrogenation to higher alcohols at 320°C , 4 MPa, GHSV of $24000 \text{ mL g}_{\text{cat}}^{-1} \text{ h}^{-1}$ and $\text{H}_2/\text{CO}_2 = 3/1$.

diffraction peaks of Cr_2O_3 species can be clearly observed in XRD patterns, only when the Cr loading reaches 3% (Fig. 5(a)). According to the STEM-EDX elemental mapping, the Cu, Fe, K and/or Cr elements are uniformly dispersed with each other over Cr(x)-CuFe catalysts (Figs. 5(e) and S8 and S9). The results of N_2 sorption exhibit that the surface area and pore volume of these Cr(x)-CuFe samples are in the range of $27.4\text{--}44.9 \text{ m}^2 \text{ g}^{-1}$ and $0.09\text{--}0.13 \text{ cm}^3 \text{ g}^{-1}$, respectively (Fig. 5(b) and Table. S4).

The surface electronic state of Cr(x)-CuFe samples was analyzed by XPS. In the Cu (2p) XPS of CuFe catalyst, the binding energies of 953.0 eV and 933.0 eV are corresponded to Cu (2p)_{1/2} and Cu (2p)_{3/2} of CuO, while those of 723.9 eV and 710.5 eV in the Fe (2p) XPS are ascribed to Fe (2p)_{1/2} and Fe (2p)_{3/2} of Fe_2O_3 (Fig. 6(a) and (b)) [34]. Doping small amount of Cr (Cr(1%)-CuFe) leads to the migration of Cu (2p) and Fe (2p) XPS signals towards higher binding energy, indicating the strong interaction of Cr promoter with CuFe catalyst. However, such a variation of Cu (2p) and Fe (2p) XPS is not evident with further increase of Cr loading. This may be because these excessive Cr additives mainly accumulate and agglomerate with each other on the surface of catalyst, thus, having weak interaction with CuFe species. It can be consolidated that the intensity of peaks at 588.5 eV and 579.4 eV, assigned to the Cr (2p)_{1/2} and Cr (2p)_{3/2} of Cr_2O_3 [35,36], is considerably enhanced, along with the attenuation of Cu (2p) XPS and Fe (2p)

XPS over Cr(2%)-CuFe and Cr(3%)-CuFe (Fig. 6). To further clarify the Cr species distribution on the CuFe catalyst surface, low-energy ion scattering (LEIS) spectra of Cr(x)-CuFe catalysts were measured (Fig. 6(d)). The Cr signal in the spectrum of Cr(x)-CuFe enhances with the Cr content, while the Fe and Cu signals significantly lower in intensity. This confirms that excessive Cr species are mainly deposited on the external surface. Moreover, the CO_2 -TPD results indicate that introduction of more Cr species substantially decreases CO_2 adsorption amount (Fig. S10). As a result, Cr(3%)-CuFe gives lower CO_2 conversion than Cr (1%)-CuFe, although they both show similar product selectivity. Nevertheless, Cr(3%)-CuFe is also stable during CO_2 hydrogenation, as indicated by its catalytic performance nearly kept at least within 24 h (Fig. S11).

The reduction and chemisorption behaviors of various Cr(x)-CuFe catalysts were evaluated by H_2 -TPR and CO -TPD. In the H_2 -TPR profiles, the peaks at $150\text{--}350^\circ\text{C}$ and above 400°C are attributed to the reduction of CuO to metal Cu and the reduction of FeO_x to metal Fe, respectively (Fig. 7(a)) [24,26]. It is worth noticing that the appearance of two hydrogen consumption peaks (centered at around 200 and 250°C respectively) in the range of $150\text{--}350^\circ\text{C}$ is originated from the different interaction of CuO with FeO_x species. Clearly, doping small amount of Cr (Cr(1%)-CuFe) intensifies the reduction peak centered at 250°C , and simultaneously make that of FeO_x to metal Fe shift towards higher temperature, indicating the enhancement of the interaction between Cu and Fe species, agreeing well with the results of XPS. The strengthened Cu-Fe interaction limits the formation of excess FeC_x generated from the carbonization of metal Fe, thus, alleviating CO over-dissociation [37]. This is verified by the CO -TPD results; the desorption peak below 150°C is due to physical absorbed CO, while those ranging from 150°C to 450°C and above 450°C correspond to mediumly and strongly chemisorbed CO on the surface of CuFe catalyst, respectively (Fig. 7(b)) [24]. Interestingly, the desorption peak of CO in the range of $150\text{--}450^\circ\text{C}$ is intensified, whereas that at above 450°C is attenuated over Cr (1%)-CuFe. The CO adsorption behaviors on the CuFe and Cr(1%)-CuFe catalysts were also investigated by CO-DRIFTS (Fig. 7(c) and (d)). The peaks at around 2130 and 2170 cm^{-1} are due to gaseous CO, whereas that at around 2020 cm^{-1} is ascribed to linearly adsorbed CO on CuFe catalyst [25,38]. Clearly, the 2020 cm^{-1} peak intensity of the Cr (1%)-CuFe is much weaker than that of the CuFe, indicative of a lower amount of linearly adsorbed CO. All these results confirm that introduction of proper amount of Cr weakens the strong adsorption of CO on CuFe catalyst, which, hence, inhibiting its over-dissociation to hydrocarbons. Indeed, a higher selectivity to $\text{C}_2\text{+OH}$ (24.9%), but lower to hydrocarbons (74.1%) were observed on Cr(1%)-CuFe than on CuFe (18.9% and 80.0% for $\text{C}_2\text{+OH}$ and hydrocarbons, respectively) (Fig. 1). Notably, excessive Cr additives can not strengthen the Cu and Fe species interaction, as they mainly accumulate and agglomerate with each other on the surface of catalyst and have weak interaction with CuFe sites. As a result, the selectivity and STY of $\text{C}_2\text{+OH}$ are decreased over Cr(2%)-CuFe and Cr(3%)-CuFe, in comparison with those of Cr(1%)-CuFe.

After reaction, the electronic structure and state of spent Cr(x)-CuFe catalysts were further investigated. The structural information of spent CuFe and Cr(1%)-CuFe was analyzed by X-ray absorption near edge structure (XANES) and extended X-ray absorption fine structure spectroscopy (EXAFS). Fe K-edge XANES spectra of the CuFe and Cr(1%)-CuFe are distinguished from those of referenced Fe foil, FeO , Fe_2O_3 and Fe_3O_4 (Fig. 8(d) and Fig. S12), due to the generation of some FeC_x species [39]. In the Fe K-edge EXAFS spectra, an intense peak at around 1.53 \AA , assigned to the Fe-O(C) coordination [23], is observed on both samples, whereas that of the Fe-Fe coordination at around 2.20 \AA is almost undetectable (Fig. 8(e)). In the Fe (2p) XPS, the peaks at 723.4 and 710.4 eV are corresponded to Fe (2p)_{1/2} and Fe (2p)_{3/2} of FeO_x species, respectively. Meanwhile, an evident peak characteristic of FeC_x species is observed in Fe (2p) XPS of spent CuFe catalyst, but it is very weak over Cr(1%)-CuFe (Fig. 8(b)) [22,37]. This is confirmed by the ^{57}Fe Mössbauer spectroscopy result; fewer amounts of FeC_x are

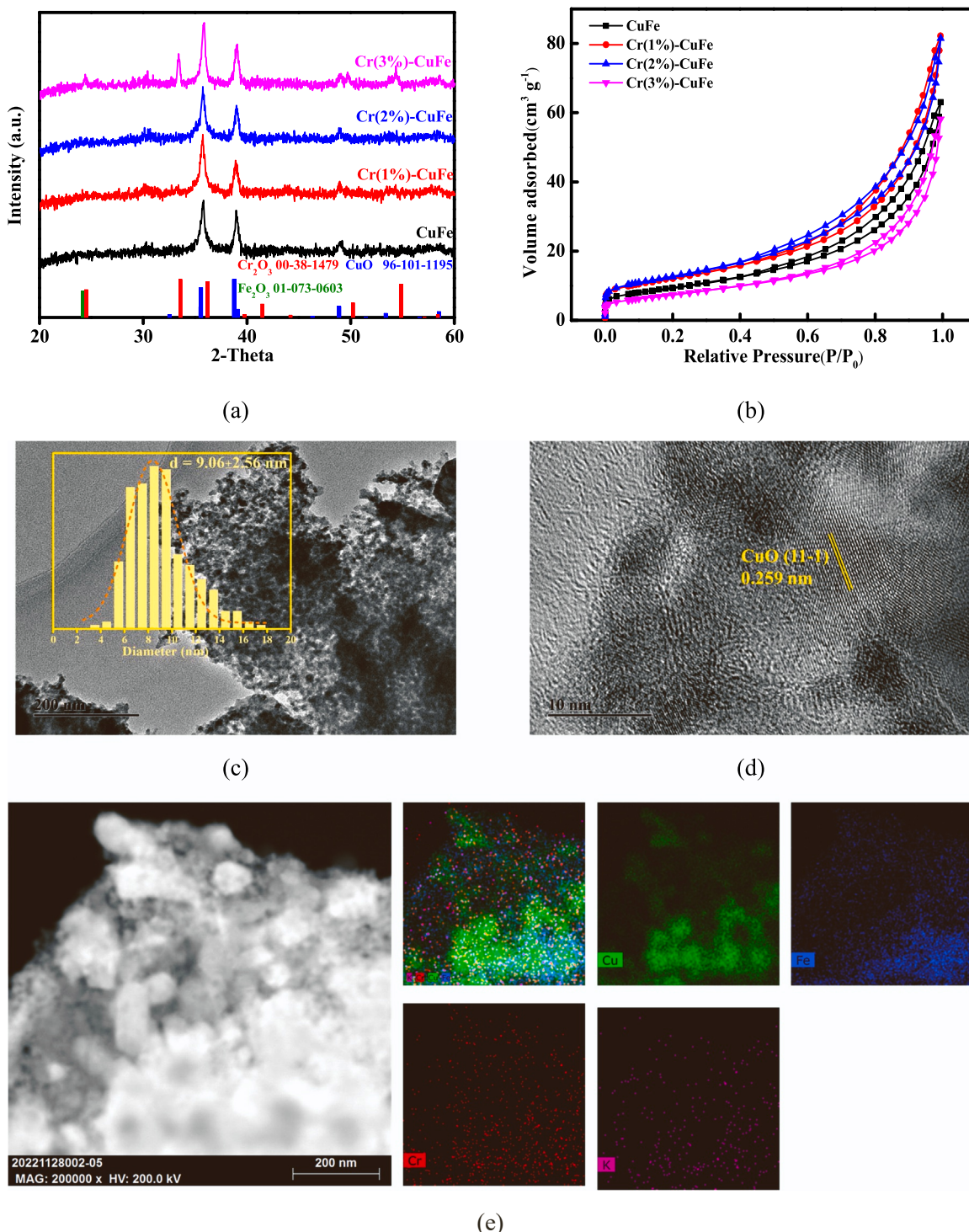


Fig. 5. XRD patterns (a), N_2 sorption isotherms (b) of $\text{Cr}(x)$ -CuFe catalysts with different Cr content, TEM image (c), HRTEM image (d) and STEM-EDX elemental mapping (e) of $\text{Cr}(1\%)$ -CuFe.

generated on $\text{Cr}(1\%)$ -CuFe (54.8%) than on CuFe (88.9%) (Fig. 8(c) and Table S5). The Cu LMM Auger electron spectra results show that $\text{Cr}(1\%)$ -CuFe has lower amounts of Cu^0 (23.2%), but higher amount of Cu^+ and Cu^{2+} (76.8%) than CuFe (30.4% of Cu^0 and 69.6% of $(\text{Cu}^+ + \text{Cu}^{2+})$) (Fig. 8(a)). All these results consolidated that doping of proper amounts of Cr enhances the interaction of Cu and Fe species, thus, inhibiting formation of FeC_x , but promoting generation of more Cu- FeC_x interfaces, which are the active sites for formation of $\text{C}_2\text{+OH}$ [26]. Fig. S13 shows that spent $\text{Cr}(1\%)$ -CuFe still possesses a uniform dispersion of Cu, Fe, Cr

and K elements, despite that the average nanoparticle size slightly increases from 9.1 nm to 12.1 nm, indicative of a high structural stability. However, the copper and iron species are obviously agglomerated over spent CuFe sample (Fig. S14).

3.3. Reaction mechanism

The reaction mechanism of CO_2 hydrogenation to higher alcohols over CuFe and $\text{Cr}(1\%)$ -CuFe catalysts was studied by *in situ* DRIFTS

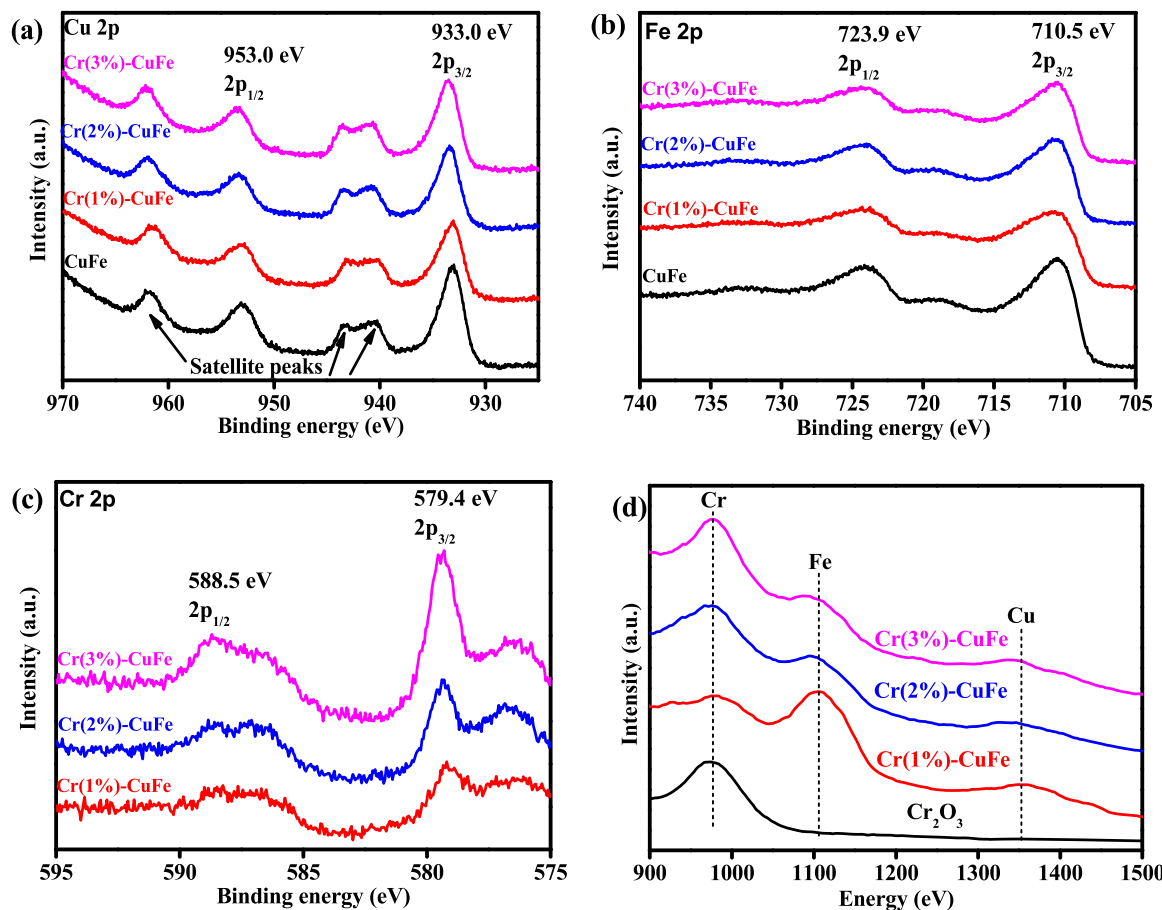


Fig. 6. Cu(2p) XPS (a), Fe(2p) XPS (b), Cr(2p) XPS (c) and LEIS spectra (d) of Cr(x)-CuFe catalysts with different Cr content.

(Fig. 9). After H_2 reduction at $400\text{ }^\circ\text{C}$ for 1 h, the temperature was dropped to $300\text{ }^\circ\text{C}$ and a mixture of H_2 and CO_2 gases (H_2 to CO_2 ratio of 3/1) was introduced into the reaction system. After reaction of 5 min, two weak peaks at 2179 and 2113 cm^{-1} , represents the generated CO intermediates, appear (Fig. 9(a)) [17,40]. Meanwhile, the peak at 1401 cm^{-1} characteristic of the C-H stretching vibration of CH_x^* species is simultaneously detected and its intensity is gradually intensified with the reaction time (Fig. 9(c)) [22,35]. The bands characteristic of formate species ($HCOO^*$) at 1590 , 2695 and 2645 cm^{-1} are also resolved (Fig. 9(e)), but their intensity is much lower than that of CH_x^* species [25]. Notably, the bands associated with acetate and acetaldehyde species are almost unobserving. These results suggest that the CO intermediates are more favorable to transform into CH_x^* species via CO dissociation activation over CuFe catalyst.

In contrast, the vibration peaks of acetate (CH_3COO^*) at 1697 cm^{-1} , 1540 cm^{-1} and 1523 cm^{-1} , and that of acetaldehyde (CH_3CHO^*) at 1749 cm^{-1} , 1737 cm^{-1} and 1716 cm^{-1} are detectable after reaction of 15 min over Cr(1%)-CuFe (Fig. 9(f)) [27,29]. The peak intensity of these acetate and acetaldehyde species is first increased up to 25 min and then decreased, indicating their further transformation into ethanol. Meanwhile, the C-H stretching vibration of CH_x^* species is considerably attenuated, along with the enhancement of the vibration peaks of adsorbed CO intermediate at 2173 , 2113 and 1928 cm^{-1} (Fig. 9(b) and (d)). This gives another piece of evidence that doping small amount of Cr effectively alleviates the over-dissociation of CO intermediate into CH_x^* species, but promotes the generation of more acetate and acetaldehyde intermediates.

We also carried out the temperature-dependent in situ DRIFTS for CO_2 hydrogenation on CuFe and Cr(1%)-CuFe catalysts (Fig. S15). The CH_x^* species at 1401 cm^{-1} is quickly produced at $170\text{ }^\circ\text{C}$ over CuFe and

its peak intensity is gradually intensified with the reaction temperature (Fig. S15(a)). Besides, the signals of formate species at 1590 and 1336 cm^{-1} are also resolved at temperature higher than $200\text{ }^\circ\text{C}$, although their intensity is lower than that of CH_x^* species. As expected, the peaks characteristic of acetate at around 1536 and 1523 cm^{-1} are very weak and they can be clearly detected, only with the temperature higher than $300\text{ }^\circ\text{C}$. As a comparison, the formation rate and the peak intensity of CH_x^* species are considerably decreased, along with the generation of more acetate and acetaldehyde intermediates on Cr(1%)-CuFe (Fig. S15(b)). The bands assigned to acetate at 1540 and 1523 cm^{-1} , and that of acetaldehyde at 1749 , 1737 and 1716 cm^{-1} quickly appear at around $250\text{ }^\circ\text{C}$ on Cr(1%)-CuFe and their intensity is much higher than that on CuFe catalyst.

Since CO_2 is generally converted to CO in CO_2 hydrogenation over Fe-based catalysts [22,24,25], the temperature programmed surface reaction (TPSR) of CO hydrogenation over these two samples were then conducted. The effluent for CO-TPSR was detected using on-line MS. The signals of acetaldehyde ($m/z = 43$) and ethanol ($m/z = 45$) are clearly visible on Cr(1%)-CuFe when the temperature is higher than $250\text{ }^\circ\text{C}$ (Fig. S16). However, the amount of generated acetaldehyde and ethanol species is significantly decreased on un-modified CuFe sample.

The adsorption of CO_2 and H_2 , and the reaction kinetics for dissociation and non-dissociation activation of CO intermediate over CuFe and Cr-modified CuFe catalysts were further evaluated by DFT calculation (Fig. 10). Cr-modified CuFe shows lower CO_2 adsorption energy (-0.44 eV) than CuFe (-0.58 eV) (Fig. 10(a)). This is in line with the CO_2 -TPD results (Fig. S17). In the CO_2 -TPD profiles, the desorption peak below $150\text{ }^\circ\text{C}$ is due to physically absorbed CO_2 , while those between 150 and $350\text{ }^\circ\text{C}$ and above $350\text{ }^\circ\text{C}$ correspond to moderately and strongly chemisorbed CO_2 respectively. Introduction of small amounts

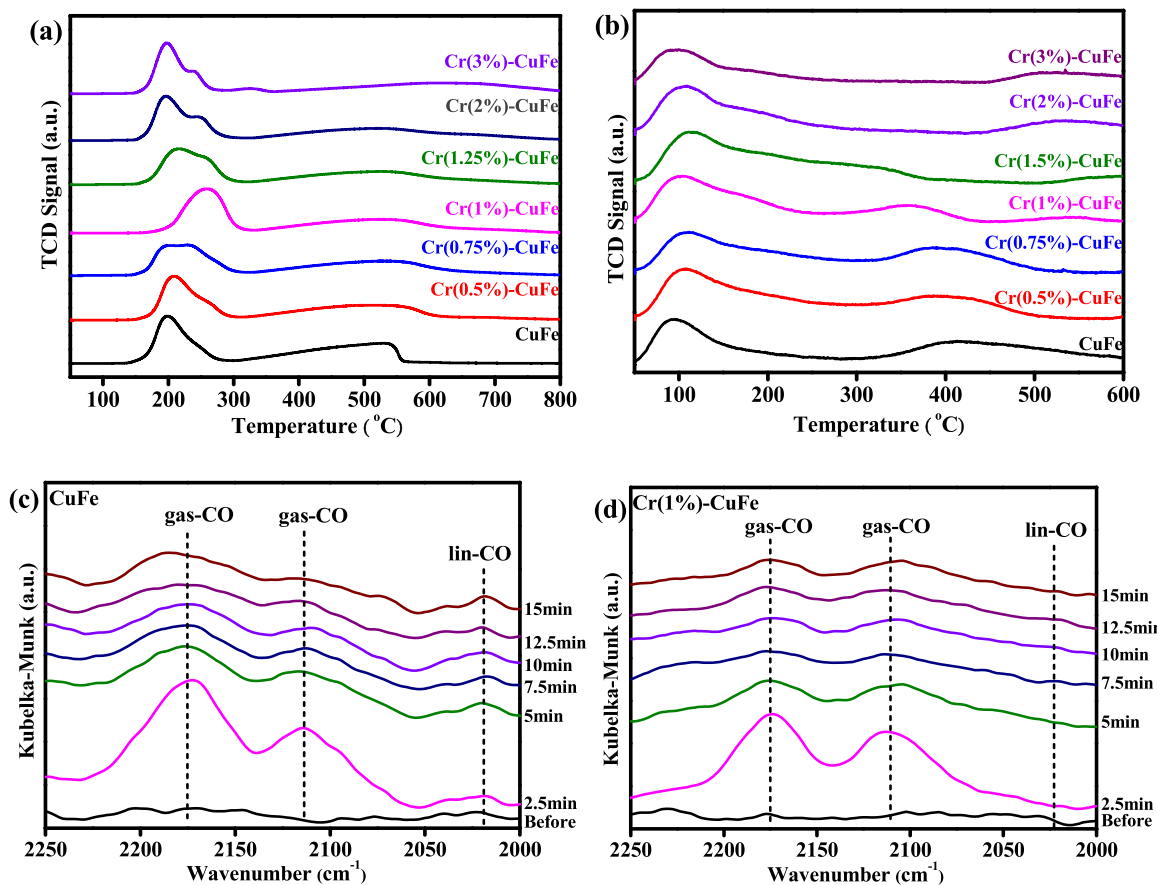


Fig. 7. H₂-TPR (a) and CO-TPD profiles (b) of CuFe and Cr(x)-CuFe, and CO-DRIFTS (c and d) of CuFe and Cr(1%)-CuFe flushed by an Ar flow (10 mL min⁻¹) for different time.

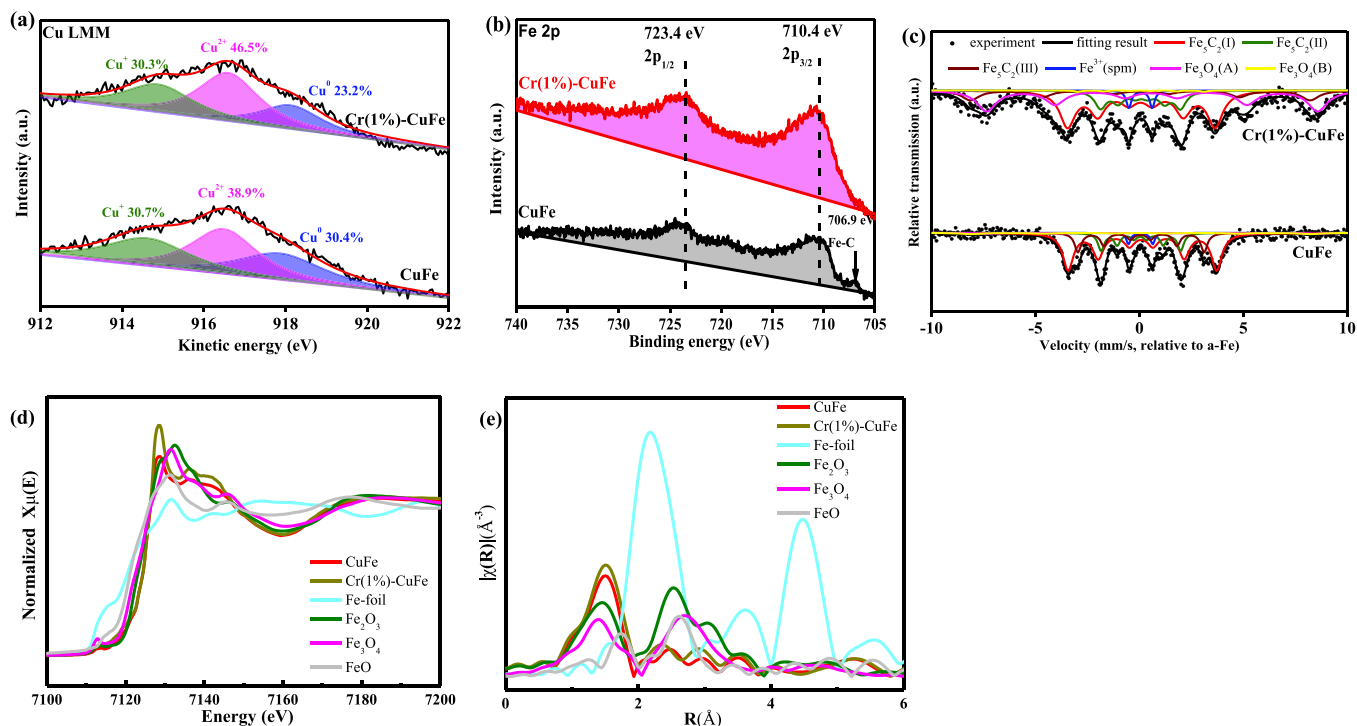


Fig. 8. Cu-LMM Auger electron spectra (a), Fe (2p) XPS (b), ⁵⁷Fe Mössbauer spectra (c) and Fe K-edge XANES (d) and EXAFS (e) of spent CuFe and Cr(1%)-CuFe catalysts.

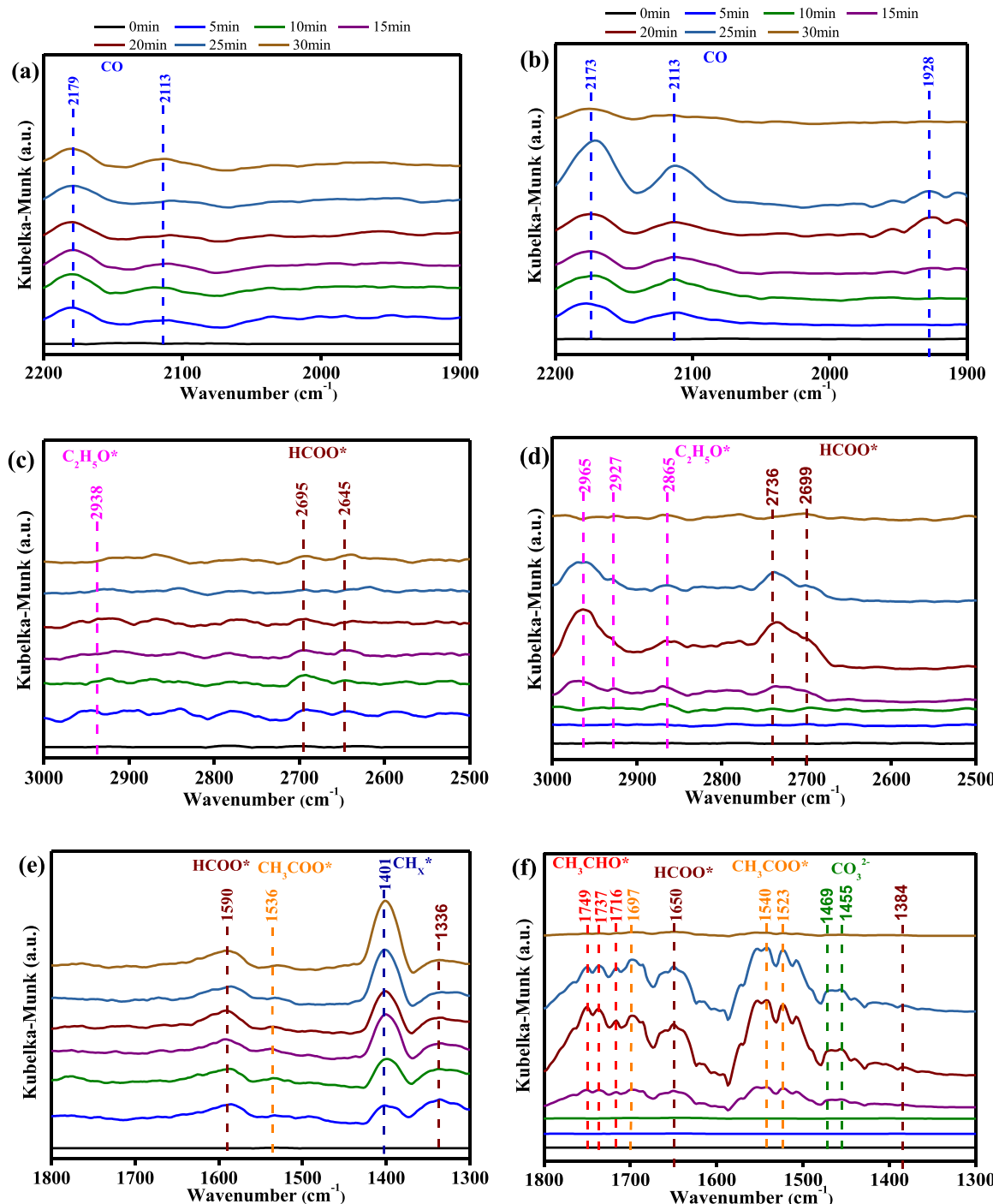


Fig. 9. In situ DRIFTS for CO_2 hydrogenation on CuFe ((a), (c) and (e)), and Cr(1%)-CuFe ((b), (d) and (f)) catalysts at $300\text{ }^\circ\text{C}$, 0.1 MPa and H_2/CO_2 of 3/1.

of Cr decreases the amount of strongly chemisorbed CO_2 , while it enhances the H_2 adsorption, as corroborated by obtaining larger H_2 adsorption energy from DFT calculations (Fig. 10(b)) and observing more intense H_2 desorption peak in the H_2 -TPD profile (Fig. S18). DFT calculations show that the adsorbed H_2 is more facilely activated on the Cr-modified CuFe due to lower H_2 dissociation energy (0.24 eV on Cr-CuFe vs. 0.37 eV on CuFe) (Fig. 10(c)). This demonstrates that doping small amounts of Cr promotes H_2 adsorption and dissociation, but weakens the CO_2 strong adsorption. It supports the hydrogen-assisted activation of CO_2 . As a result, a higher CO_2 conversion was obtained on Cr(1%)-CuFe than on CuFe (Fig. 1).

Moreover, direct dissociation of CO intermediate over CuFe catalyst

requires energy barriers of 1.22 eV, which is lower than that over Cr-modified CuFe catalyst (2.34 eV) (Fig. 10 (d)). However, interaction of CH_x with non-dissociated CO to form acetate is more favorable on Cr-modified CuFe than on CuFe, as the energy barrier (1.54 eV) of the former is lower than that of the latter (1.99 eV) (Fig. 10 (e)). This is in line with the observation of in situ DRIFTS that more acetate species are produced on Cr(1%)-CuFe (Figs. 9 and S15).

In a word, the prepared Cr-modified CuFe (Cr(1%)-CuFe) catalyst showed higher CO_2 conversion, and the selectivity and STY of $\text{C}_2\text{+OH}$ than those of the un-modified sample in CO_2 hydrogenation to higher alcohols. The results of XRD, TEM and STEM-EDX elemental mapping indicate that introduction of small amount of Cr has less influence on the

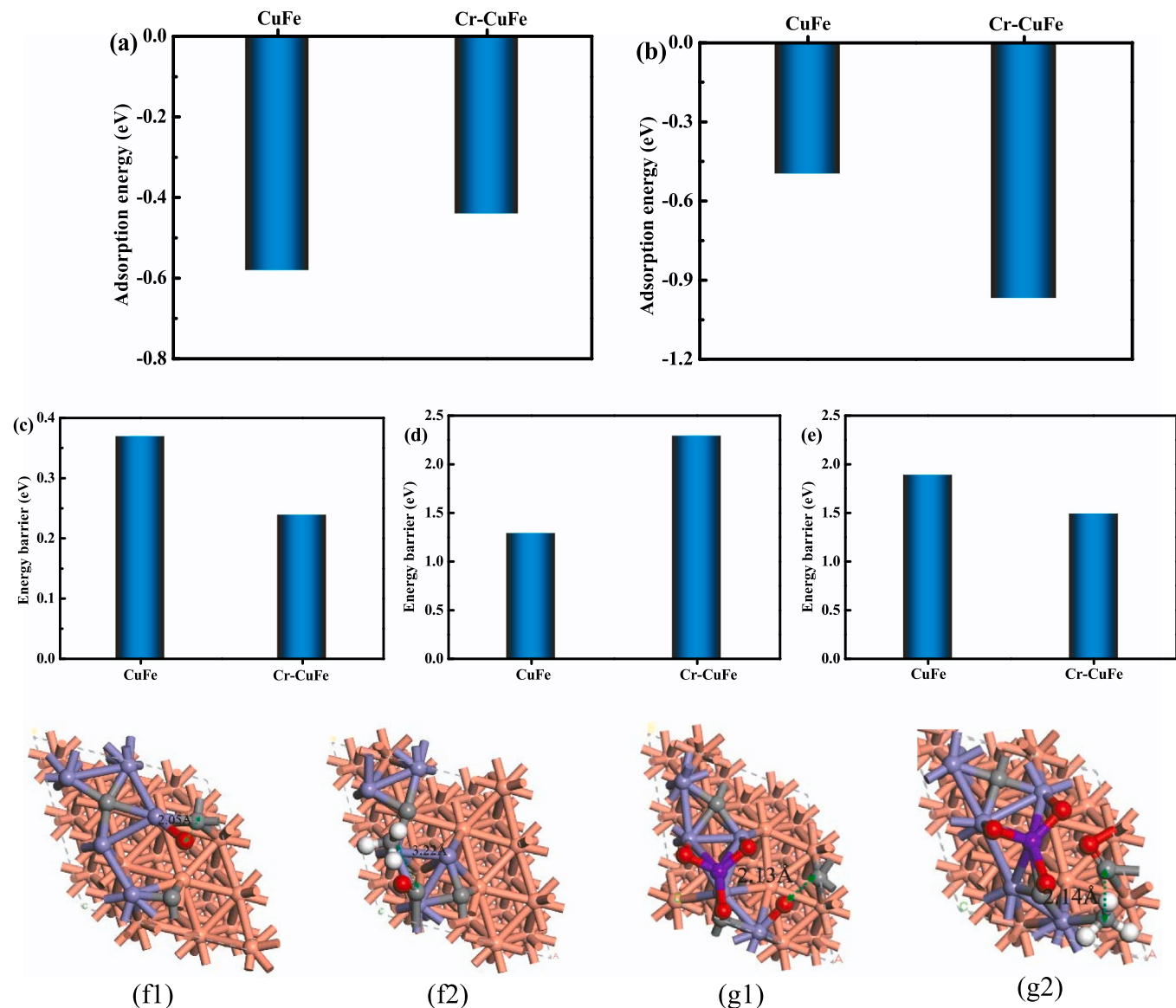


Fig. 10. Calculated adsorption energy of CO₂ (a) and H₂ (b), and the energy barrier for H₂ dissociation (c), CO dissociation (d) and interaction of CO with CH₃* (e) over CuFe and Cr-modified CuFe catalysts. Optimized transition states of CO dissociation (1) and interaction of CO with CH₃* (2) over CuFe (f) and Cr-modified CuFe (g) catalysts. Atomic coloring: O (red), C (grey), Cu (orange), Fe (blue) and Cr (purple).

crystal structure of fresh CuFe catalysts, with the Cu, Fe, K and Cr elements uniformly dispersed with each other. H₂-TPD, CO₂-TPD and DFT calculation suggest that Cr promoters can improve the H₂ adsorption and activation, but weakens the over-strong adsorption of CO₂, which, hence, promoting the hydrogen-assisted activation of CO₂. Meanwhile, doping small amount of Cr (Cr(1%)-CuFe) enhanced the interaction between Cu and Fe species that limits the formation of excess FeC_x generated from the carbonization of metal Fe, thus, alleviating CO over-dissociation.

4. Conclusion

In this work, various Cr-modified CuFe (Cr(x)-CuFe) catalysts were fabricated and tested for hydrogenation of CO₂ to higher alcohol (C₂₊OH). The CO₂ conversion, and the selectivity and STY of C₂₊OH over Cr(1%)-CuFe reached 38.4%, 29.2% and 104.1 mg g_{cat}⁻¹ h⁻¹, respectively, at 320 °C, 4.0 MPa and 6000 mL g⁻¹ h⁻¹. At higher space velocity of 48000 mL g⁻¹ h⁻¹, the STY of C₂₊OH can be further increased to 268.5 mg g_{cat}⁻¹ h⁻¹, being much higher than most of the

results in literature. More importantly, no evident deactivation was observed over Cr(1%)-CuFe catalyst even after reaction of 120 h at different space velocities. The crystal structure, elemental distribution and surface electronic states of Cr(x)-CuFe catalysts and their reaction mechanism in CO₂ hydrogenation to C₂₊OH were systematically investigated by XRD, XPS, LEIS, TEM/HR-TEM, STEM-EDX elemental mapping, H₂-TPR, H₂/CO₂/CO-TPD, XANES/EXAFS, ⁵⁷Fe Mössbauer spectra, in situ DRIFTS and DFT calculation. It was confirmed that doping proper amount of Cr strengthens the interaction between Cu and Fe species, which inhibits the production of excessive iron carbide species and alleviates CO over-dissociation (Fig. 11). In contrast, more acetate and acetaldehyde intermediates are produced via promoting the interaction of CH_x with non-dissociated CO over Cu-FeC_x interface. This work not only provides an efficient modified CuFe catalyst for CO₂ hydrogenation to C₂₊OH, but also clarifies the key role of Cr additive in promoting higher alcohols formation.

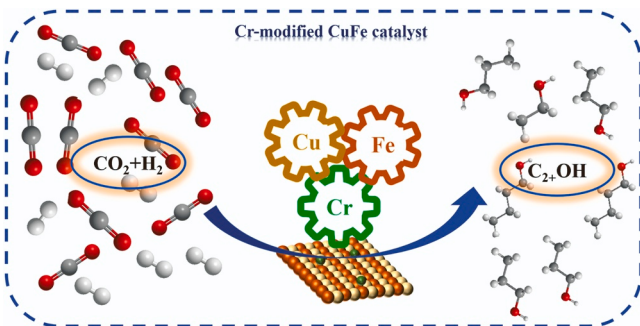


Fig. 11. Reaction scheme for CO_2 hydrogenation to C_{2+}OH over Cr-modified CuFe catalyst.

CRediT authorship contribution statement

Qian Zhang: Conceptualization, Methodology, Investigation, Formal analysis, Writing – original draft. **Sen Wang:** Conceptualization, Methodology, Investigation, Formal analysis, Funding acquisition, Writing – review & editing. **Rui Geng:** Methodology, Investigation. **Pengfei Wang:** Methodology, Investigation. **Mei Dong:** Conceptualization, Funding acquisition. **Jianguo Wang:** Conceptualization, Funding acquisition. **Weibin Fan:** Supervision, Conceptualization, Funding acquisition, Writing – review & editing.

Declaration of Competing Interest

The authors declare that they have no known competing financial interests or personal relationships that could have appeared to influence the work reported in this paper.

Data availability

Data will be made available on request.

Acknowledgements

The authors sincerely thank to the financial supports of National Key R&D Program of China (2020YFA0210900), National Natural Science Foundation of China (U1910203; 21991090; 21991092; 22272195; U22A20431), Natural Science Foundation of Shanxi Province of China (202203021224009), Innovation foundation of Institute of Coal Chemistry, Chinese Academy of Sciences (SCJC-DT-2023-06); Youth Innovation Promotion Association CAS (2021172). The authors thank Shanghai Synchrotron Radiation Facility (SSRF) beamline for XAS experimental data collection.

Appendix A. Supporting information

Supplementary data associated with this article can be found in the online version at [doi:10.1016/j.apcatb.2023.123013](https://doi.org/10.1016/j.apcatb.2023.123013).

References

- Trends in Atmospheric Carbon Dioxide : Full Record. ESRL Global Monitoring Division, Global Greenhouse Gas Reference Network, NOAA. <https://gml.noaa.gov/ccgg/trends/global.html> (accessed Feb 13, 2023).
- J. Rogelj, M.D. Elzen, N. Höhne, T. Fransen, H. Fekete, H. Winkler, R. Schaeffer, F. Sha, K. Riahi, M. Meinshausen, Paris Agreement climate proposals need a boost to keep warming well below 2 °C, *Nature* volume 534 (2016).
- S.J. Davis, K. Caldeira, H.D. Matthews, Future CO_2 emissions and climate change from existing energy infrastructure, *Science* 329 (2010) 1330–1333.
- N.M. Dowell, P.S. Fennell, N. Shah, G.C. Maitland, The role of CO_2 capture and utilization in mitigating climate change, *Nat. Clim. Change* 7 (2017) 243.
- L.K. Wang, Y. Han, J. Wei, Q.J. Ge, S.J. Lu, Y.P. Mao, J. Sun, Dynamic confinement catalysis in Fe-based CO_2 hydrogenation to light olefins, *Appl. Catal. B* 328 (2023), 122506.
- W.Y. Zhang, S. Wang, S.J. Guo, Z.F. Qin, M. Dong, J.G. Wang, W.B. Fan, Effective conversion of CO_2 into light olefins along with generation of low amounts of CO , *J. Catal.* 413 (2022) 923–933.
- W. Li, G.W. Zhan, X.B. Liu, Y.H. Yue, K.B. Tan, J. Wang, J.L. Huang, Q.B. Li, Assembly of ZnZrOx and ZSM-5 on hierarchically porous bio-derived SiO_2 platform as bifunctional catalysts for CO_2 hydrogenation to aromatics, *Appl. Catal. B* 330 (2023), 122575.
- S. Kattel, P.J. Ramirez, G.J.G. Chen, J.A. Rodriguez, P. Liu, Active sites for CO_2 hydrogenation to methanol on Cu/ZnO catalysts, *Science* 355 (2017) 1296–1299.
- J. Wei, R.W. Yao, Q.J. Ge, Z.Y. Wen, X.W. Ji, C.Y. Fang, J.X. Zhang, H.Y. Xu, J. Sun, Catalytic hydrogenation of CO_2 to isoparaffins over Fe-based multifunctional catalysts, *ACS Catal.* 8 (2018) 9958–9967.
- S. Wang, L. Zhang, P.F. Wang, W.Y. Jiao, Z.F. Qin, M. Dong, J.G. Wang, U. Olsbye, W.B. Fan, Highly selective hydrogenation of CO_2 to propane over $\text{GaZrO}_x/\text{H-SSZ-13}$ composite, *Nat. Catal.* 5 (2022) 1038–1050.
- A.H.M.D. Silva, L.H. Vieira, C.S. Santana, M.T.M. Koper, E.M. Assaf, J.M. Assaf, J. F. Gomes, Ethanol formation from CO_2 hydrogenation at atmospheric pressure using Cu catalysts: Water as a key component, *Appl. Catal. B* 324 (2023), 122221.
- J. Artz, T.E. Müller, K. Thernert, Sustainable conversion of carbon dioxide: An integrated review of catalysis and life cycle assessment, *Chem. Rev.* 118 (2018) 434–504.
- S.N. Zhang, Z.X. Wu, X.F. Liu, Z.L. Shao, L. Xia, L.S. Zhong, H. Wang, Y.H. Sun, Tuning the interaction between Na and Co_2C to promote selective CO_2 hydrogenation to ethanol, *Appl. Catal. B* 293 (2021), 120207.
- F. Zeng, C. Mebrahtu, X.Y. Xi, L.F. Liao, J. Ren, J.X. Xie, H.J. Heeres, R. Palkovits, Catalysts design for higher alcohols synthesis by CO_2 hydrogenation: Trends and future perspectives, *Appl. Catal. B* 291 (2021), 120073.
- D. Xu, Y.Q. Wang, M.Y. Ding, X.L. Hong, G.L. Liu, S.C.E. Tsang, Advances in higher alcohol synthesis from CO_2 hydrogenation, *Chem* 7 (2020) 849–881.
- K. An, S.R. Zhang, H. Wang, N.Y. Li, Z.Y. Zhang, Y. Liu, $\text{Co}^0\text{-Co}^{\delta+}$ active pairs tailored by Ga-Al-O spinel for CO_2 -to-ethanol synthesis, *Chem. Eng. J.* 433 (2022), 134606.
- S.N. Zhang, X.F. Liu, Z.L. Shao, H. Wang, Y.H. Sun, Direct CO_2 hydrogenation to ethanol over supported Co_2C catalysts: Studies on support effects and mechanism, *J. Catal.* 382 (2020) 86–96.
- L.P. Ding, T.T. Shi, J. Gu, Y. Cui, Z.Y. Zhang, C.J. Yang, T. Chen, M. Lin, P. Wang, N.H. Xue, L.M. Peng, X.F. Guo, Y. Zhu, 1 Z. X. Chen, W. P. Ding, CO_2 hydrogenation to ethanol over $\text{Cu}@\text{Na-Beta}$, *Chem* 6 (2020) 2673–2689.
- F.J. Caparrós, L. Soler, M.D. Rossell, I. Angurell, L. Piccolo, O. Rossell, J. Llorca, Remarkable carbon dioxide hydrogenation to ethanol on a palladium/iron oxide single-atom catalyst, *ChemCatChem* 10 (2018) 2365–2369.
- B. Ouyang, S.H. Xiong, Y.H. Zhang, B. Liu, J.L. Li, The study of morphology effect of $\text{Pt}/\text{Co}_3\text{O}_4$ catalysts for higher alcohol synthesis from CO_2 hydrogenation, *Appl. Catal. A* 543 (2017) 189–195.
- Y. Lou, F. Jiang, W. Zhu, L. Wang, T.Y. Yao, S.S. Wang, B. Yang, B. Yang, Y.F. Zhu, X.H. Liu, CeO_2 supported Pd dimers boosting CO_2 hydrogenation to ethanol, *Appl. Catal. B* 291 (2021), 120122.
- Z.Y. Si, L.K. Wang, Y. Han, J.F. Yu, Q.J. Ge, C.Y. Zeng, J. Sun, Synthesis of Alkene and Ethanol in CO_2 Hydrogenation on a Highly Active Sputtering CuNaFe Catalyst, *ACS Sustain. Chem. Eng.* 10 (2022) 14972–14979.
- Y. Wang, K.Z. Wang, B.Z. Zhang, X.B. Peng, X.H. Gao, G.H. Yang, H. Hu, M.B. Wu, N. Tsubaki, Direct conversion of CO_2 to ethanol boosted by intimacy-sensitive multifunctional catalysts, *ACS Catal.* 11 (2021) 1742–11753.
- D. Xu, M. Ding, X. Hong, G. Liu, Mechanistic aspects of the role of K promotion on Cu-Fe-based catalysts for higher alcohol synthesis from CO_2 hydrogenation, *ACS Catal.* 10 (2020) 14516–14526.
- D. Xu, H. Yang, X. Hong, G.L. Liu, S.C. Edman, Tsang, Tandem catalysis of direct CO_2 hydrogenation to higher alcohols, *ACS Catal.* 11 (2021) 8978–8984.
- D. Xu, M. Ding, X. Hong, G. Liu, S.C.E. Tsang, Selective C_{2+} alcohol synthesis from direct CO_2 hydrogenation over a Cs-promoted Cu-Fe-Zn catalyst, *ACS Catal.* 10 (2020) 5250–5260.
- Y.Q. Wang, X.X. Zhang, X.L. Hong, G.L. Liu, Sulfate-promoted higher alcohol synthesis from CO_2 hydrogenation, *ACS Sustain. Chem. Eng.* 10 (2022) 8980–8987.
- H.J. Guo, S.G. Li, F. Peng, H.R. Zhang, L. Xiong, C. Huang, C. Wang, X.D. Chen, Roles investigation of promoters in K/Cu-Zn catalyst and higher alcohols synthesis from CO_2 hydrogenation over a novel two-stage bed catalyst combination system, *Catal. Lett.* 145 (2015) 620–630.
- Y. Wang, D. Xu, X. Zhang, X. Hong, G.L. Liu, Selective C_{2+} alcohol synthesis by CO_2 hydrogenation via a reaction-coupling strategy, *Catal. Sci. Technol.* 12 (2022) 1539–1550.
- G. Kresse, J. Hafner, Ab initio molecular dynamics simulation of the liquid metal amorphous semiconductor transition in germanium, *Phys. Rev. B Condens. Matter* 49 (1994) 14251–14269.
- J.P. Perdew, K. Burke, M. Ernzerhof, Generalized gradient approximation made simple, *Phys. Rev. Lett.* 77 (1996) 3865–3868.
- K. Mori, H. Hata, H. Yamashita, Interplay of Pd ensemble sites induced by GaO_x modification in boosting CO_2 hydrogenation to formic acid, *Appl. Catal. B* 320 (2023), 122022.
- G. Henkelman, H. Jonsson, Improved tangent estimate in the nudged elastic band method for finding minimum energy paths and saddle points, *J. Chem. Phys.* 113 (2000) 9978–9985.
- Y.W. Lu, R.G. Zhang, B.B. Cao, B.H. Ge, F.F. Tao, J.J. Shan, L. Nguyen, Z.H. Bao, T. P. Wu, J.W. Pote, B.J. Wang, F. Yu, Elucidating the copper–hägg iron carbide synergistic interactions for selective CO hydrogenation to higher alcohols, *ACS Catal.* 7 (2017) 5500–5512.

[35] S. Wang, L. Z, P.F. Wang, X.C. Liu, Y.Y. Chen, Z.F. Qin, M. Dong, J.G. Wang, L. He, U. Olsbye, W.B. Fan, Highly effective conversion of CO₂ into light olefins abundant in ethene, in: *Chem.*, 8, 2022, pp. 1376–1394.

[36] X.F. Gao, Y.Q. Wu, T. Zhang, L.Y. Wang, X.L. Li, H.J. Xie, Y.S. Tan, Binary ZnO/Zn–Cr nanospinel catalysts prepared by a hydrothermal method for isobutanol synthesis from syngas, *Catal. Sci. Technol.* 8 (2018) 2975–2986.

[37] R. Yao, J. Wei, Q. Ge, J. Xu, Y. Han, Q. Ma, H. Xu, J. Sun, Monometallic iron catalysts with synergistic Na and S for higher alcohols synthesis via CO₂ hydrogenation, *Appl. Catal. B* 298 (2021), 120556.

[38] T.K. Liu, D. Xu, M.Y. Song, X.L. Hong, G.L. Liu, K–ZrO₂ interfaces boost CO₂ hydrogenation to higher alcohols, *ACS Catal.* 13 (2023) 4667–4674.

[39] K. Gong, Y. Wei, T.J. Lin, X.Z. Qi, F.F. Sun, Z. Jiang, L.S. Zhong, Maximizing the interface of dual active sites to enhance higher oxygenate synthesis from syngas with high activity, *ACS Catal.* 13 (2023) 4533–4543.

[40] G.C. Zhang, G.L. Fan, L.R. Zheng, F. Li, Ga-Promoted CuCo-Based Catalysts for Efficient CO₂ Hydrogenation to Ethanol: The Key Synergistic Role of Cu-CoGaO_x Interfacial Sites, *ACS Appl. Mater. Inter.* 14 (2022) 35569–35580.